Quantifying the impact of urban geometric detail for urban air mobility risk forecasting

Patil, Akshay; García-Sánchez, Clara

DOI
10.1016/j.scs.2025.106750

Publication date
2025

Document Version
Final published version

Published in
Sustainable Cities and Society

Citation (APA)
Patil, A., & García-Sánchez, C. (2025). Quantifying the impact of urban geometric detail for urban air mobility risk forecasting. *Sustainable Cities and Society*, *132*, Article 106750. https://doi.org/10.1016/j.scs.2025.106750

Sustainable Cities and Society 132 (2025) 106750

Contents lists available at ScienceDirect

Sustainable Cities and Society

journal homepage: www.elsevier.com/locate/scs

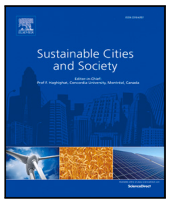

Quantifying the impact of urban geometric detail for urban air mobility risk forecasting

Akshay Patil *, Clara García-Sánchez

3D Geoinformation Research Group, Faculty of Architecture and the Built Environment, Delft University of Technology, Building 8, Julianalaan 134, Delft, 2628BL, The Netherlands

ARTICLE INFO

Keywords:
Computational fluid dynamics
RANS
Urban-air mobility
OpenFOAM
Level of detail (LoD)
Urban fluid dynamics

ABSTRACT

Wind flow predictions in realistic urban areas are sensitive to a wide range of governing parameters such as building resolution, wind incidence, urban morphology, and underlying topography, to name a few. In this study, we systematically study the impact of the geometric level of detail (LoD) of the urban built environment using a Reynolds Averaged Navier–Stokes (RANS) computational framework specifically tailored for urban air mobility. Using a wind-incidence angular resolution of 1°, we simulated a total of 1440 simulations for two distinct urban areas and developed a probabilistic risk metric ($\mathcal{P}^r$) based on velocity and turbulence fields that allow us to compare the impact of LoD 1.2 (lower geometric detail) and LoD 2.2 (higher geometric detail). Comparing the wind-rose weighted average velocity and the risk map, we found that LoD 2.2 provides a more conservative prediction for high-risk areas than LoD 1.2, suggesting the need to adopt higher geometric details when applicable. Our results present a cautionary view on the impact of LoD and how automatic reconstruction can further the efficiency of current wind engineering practices.

1. Introduction

The need for understanding the impact of wind prediction in the urban built environment has accelerated in recent years to envision, improve, and support the development of sustainable and climate-conscious urban planning (Blocken, 2015). The disproportionate concentration of economic and social activities and infrastructure within the urban built environment in almost all major urban centres in the world has imparted a unique resource strain on the modern urban built environment. As urban centres in the world take up more land to accommodate for the increasing population density (Güneralp, Reba, Hales, Wentz, & Seto, 2020; McDonald et al., 2020), complex and historically rooted zoning laws coupled with the limited horizontal space have led to the growth of taller buildings in urban areas, thus exacerbating wind-comfort and peak wind loading issues (Ciarlatani, Huang, Philips, & Gorlé, 2023; Hochschild & Gorlé, 2024a, 2024b; Pomaranzin et al., 2022). Accurate wind prediction in such dense urban environments is therefore critical for evaluating pedestrian wind comfort, structural safety, and the aerodynamic implications for emerging technologies such as urban air mobility systems.

In parallel, air quality (specifically SO_2, NO_x, O_3, $PM_{2.5}$, PM_{10}, to list a few) globally became progressively worse until 2018 (Fowler et al., 2020). At this point, the most recent concrete emissions control was undertaken to improve the air quality in urban areas. Wolf, Pettersson, and Esau (2020) conducted a high-resolution study in the city of Bergen, Norway, and found that poor urban air quality and particulate matter (PM2.5) can be attributed primarily to road traffic. Another study commissioned by the European Parliament found similarly concerning levels of air quality in urban environments (Nagl, Buxbaum, Bohmer, Ibesich, & Mendoza, 2018), and recently lowered the permissible levels for particulate matter, SO_x, NO_x, O_3, and PM2.5 (C. of the European Union, 2023), illustrating a pressing need to better understand, predict, and combat worsening air quality. One potential solution to alleviate poor air quality in urban areas that has been proposed is to eliminate traditional last-mile transit modes and supplement these with Unmanned Aerial Vehicles (UAVs) or drones (Cui, Yang, Gao, Cui, & Najafi, 2024; Elsayed & Mohamed, 2020). Lemardelé, Estrada, Pagès, and Bachofner (2021) explored various drone last-mile transit options to quantify the financial feasibility of using air delivery coupled with traditional transit options in European cities like Barcelona, Spain and Paris, France. While drones can be designed to actively avoid extreme wind events, including wind gusts, turbulence, and shear winds, to name a few (Cho et al., 2019; Tran, Santoso, & Garratt, 2021; Xing, Zhang, & Su, 2023), identifying the urban areas that have a relatively large probability for such events can help with better trajectory planning. One of the significant factors in deciding the

* Corresponding author.
E-mail address: a.l.patil@tudelft.nl (A. Patil).

https://doi.org/10.1016/j.scs.2025.106750
Received 8 May 2025; Received in revised form 18 August 2025; Accepted 18 August 2025
Available online 8 September 2025

viability of such a drone delivery system in dense urban areas is the incident wind conditions, which can severely affect the battery drain rate for small- to medium-sized drones (Galkin, Kibilda, & DaSilva, 2019). Moreover, they found that statistically characterising the potential risk of traversing a given neighbourhood can provide substantial benefits when deciding the route.

As detailed above, understanding the wind flow within the urban canopy can help resolve a wide range of problems from pedestrian wind comfort to air quality, which are directly impacted by the complex transport processes therein (Collett & Oduyemi, 1997). However, predicting the wind conditions in a complex urban environment involves many challenges that have been concisely summarised by Blocken (2015). These challenges include strong flow variability at multiple spatial and temporal scales, the presence of sharp geometric discontinuities, high turbulence intensities, and the difficulty of obtaining accurate boundary and validation data. Among these, urban morphology plays a dominant role because it directly governs the spatial structure of the built environment, which in turn dictates the flow separation, recirculation zones, and channelling effects that are central to urban wind dynamics. Understanding the response of the urban environment to changing boundary conditions (in this case, wind-incidence angle) is still poorly understood due to the wide variety of urban morphology. In this case, the definition of urban morphology is confined to the spatial context as discussed in Biljecki and Chow (2022), Boeing (2018) and Labetski, Vitalis, Biljecki, Ohori, and Stoter (2023), where the urban form does not constitute a single metric but a collection of multiple metrics, including the layout of the street network, building heights, and building clusters, among others (Labetski et al., 2023).

Numerous studies have shown that variables such as urban density, plan and frontal area densities, canyon ratios, and building aspect ratios affect flow patterns (Carpentieri & Robins, 2015; Hang, Sandberg, & Li, 2009; Karimimoshaver, Khalvandi, & Khalvandi, 2021; Palusci, Monti, Cecere, Montazeri, & Blocken, 2021). However, accurately characterising urban morphology requires identifying which of these many parameters has a dominant influence. Even if only a small subset — say 5% — of the proposed 300 metrics are of first-order importance, at least 15 parameters would need to be considered for fair comparisons. This highlights the need for a well-defined and consistent framework for describing urban form, which remains an ongoing challenge. One such standard is the Level of Detail (LoD), which offers a clear, hierarchical structure for representing building geometry (Biljecki, Ledoux, & Stoter, 2016), which also constitutes a central challenge in data acquisition (Mirzaei, 2021). Each higher LoD level incrementally refines the geometric description (see Fig. 1), converging toward the true structure and enabling consistent differentiation of the built environment for wind simulations and related applications (Biljecki et al., 2016).

Specifically, in the context of LoD 1.2 and LoD 2.2, one of the central distinguishing characteristics is the attribution of multiple building heights for a single building footprint. For LoD 1.2, each building footprint is restricted to have a unique height attribute, while for LoD 2.2, this is not the case, as clearly depicted in Fig. 1(b)–(e). This restriction of single building height also limits LoD 1.2 from representing sloped or slanting roofs, as well as tall features such as chimneys and towers, as seen when comparing Fig. 1(b) and (d) to (c) and (e). For a detailed description of the differences between the considered LoD's, the discussion presented in Biljecki et al. (2016) can be consulted along with figure 3 therein. This limitation can lead to a substantial under-representation of the true building height distribution in urban environments. Despite recent efforts to extend the LoD framework to better capture these complexities (van der Vaart et al., 2024), the original LoD definition remains a robust foundation for urban fluid dynamics applications, particularly in light of other leading-order uncertainties such as mesh complexity and data availability.

Motivated by the above discussion, In this paper, we systematically studied the effect of building LoD (i.e., geometric level of detail) on the wind flow predictions both at the pedestrian level and the UAV operation level through the use of two distinct LoDs and two distinct urban environments with a wind incidence angular resolution of 1° resulting in a total of 1440 simulations (360 simulation per case with a total of 4 cases). Specifically, for the first time in the literature, we present a systematic investigation on the impact of LoD 1.2, which only allows for a single building height per building footprint (industry standard), against a relatively higher geometric detail LoD 2.2 (see Fig. 1). Here, the primary goal is to illustrate the effect of LoD on the predicted flow metrics and not to develop a recommendation on the minimum level of LoD required for a given application. Additionally, this study is not aimed at validating the current computational methodology against in situ measurements, as validation data does not yet exist. The following sections describe the computational methodology, mesh design, grid convergence, and boundary condition setup in Section 2. This is followed by presenting the results for the two cases considered in Section 3. Finally, in Section 4, we present the concluding remarks and future directions.

2. Methods

2.1. Governing equations and discretisation

This paper uses the steady-state Reynolds-Averaged Navier–Stokes (RANS) momentum equations constrained by the incompressible flow assumption to obtain the wind field within the urban environment. The governing equations are given by

$$\partial_j \overline{u_j u_i} = -\frac{1}{\rho}\partial_i \overline{p} + \nu \partial_j \partial_j \overline{u_i} + \partial_j \overline{u_j' u_i'}, \tag{1}$$

and

$$\partial_i \overline{u_i} = 0, \tag{2}$$

where ρ is the density of the fluid, which is assumed to be constant, ν is the kinematic viscosity of the fluid ($\nu_{\text{air}} = 10^{-5}$ m^2/s), $\overline{u}_i$ represents the Reynolds-averaged velocity, $\overline{p}$ is the pressure, and $\partial_j \overline{u_j' u_i'}$ are the Reynolds-stress' that constitute the closure problem for incompressible fluid flow equations described in Eqs. (1) and (2) where u_i' represents the fluctuating component of the velocity. In the equations above, we use the tensorial index notation, where repeating indices are summed over unless mentioned otherwise. Specifically, the conventional partial differential operator $\partial\langle\cdot\rangle/\partial x$ is equivalent to $\partial_1\langle\cdot\rangle$ and $j = 1, 2, 3$ corresponds to x, y, and z coordinate axes, respectively. Here, the x and y directions correspond to the horizontal directions, while the z axis corresponds to the vertical direction using a right-handed coordinate system. The system of equations is mathematically closed using the Boussinesq eddy-viscosity hypothesis that relates the Reynolds-stress to the mean rate of strain via the linear eddy viscosity using the $k-\epsilon$ turbulence closure equation (Launder & Spalding, 1974) where $k = \overline{u_i' u_i'}/2$ is the turbulent kinetic energy (TKE) and $\epsilon = \nu \overline{\partial_j u_i' \partial_i u_j'}$ is the TKE dissipation rate. Specifically, the standard variant (Launder & Spalding, 1974) of the two-equation closure is used to solve the transport equations given by

$$\partial_j k \overline{u}_i = \partial_j \left(\nu + \frac{\nu_t}{\sigma_k} \partial_j k \right) + P_k - \epsilon + S_k, \tag{3}$$

and

$$\partial_j \epsilon \overline{u}_i = \partial_j \left(\nu + \frac{\nu_t}{\sigma_\epsilon} \partial_j \epsilon \right) + C_{1,\epsilon} S_\epsilon - C_{2,\epsilon} \frac{\epsilon^2}{k + \sqrt{\nu \epsilon}} + S_\epsilon, \tag{4}$$

where, Eqs. (3) and (4) are the transport equations for k and ϵ, respectively. Here $\sigma_k = 1.0$, $\sigma_\epsilon = 1.3$, $C_{1,\epsilon} = 1.44$, and $C_{2,\epsilon} = 1.92$ are model constants that have an empirical origin to close the transport equations for k and ϵ. While P_k is the production of TKE, S_k is a sink of TKE, and S_ϵ is the sink term for the TKE dissipation rate. The turbulent/eddy-viscosity (ν_t) is computed as

$$\nu_t = C_\mu \frac{k^2}{\epsilon}, \tag{5}$$

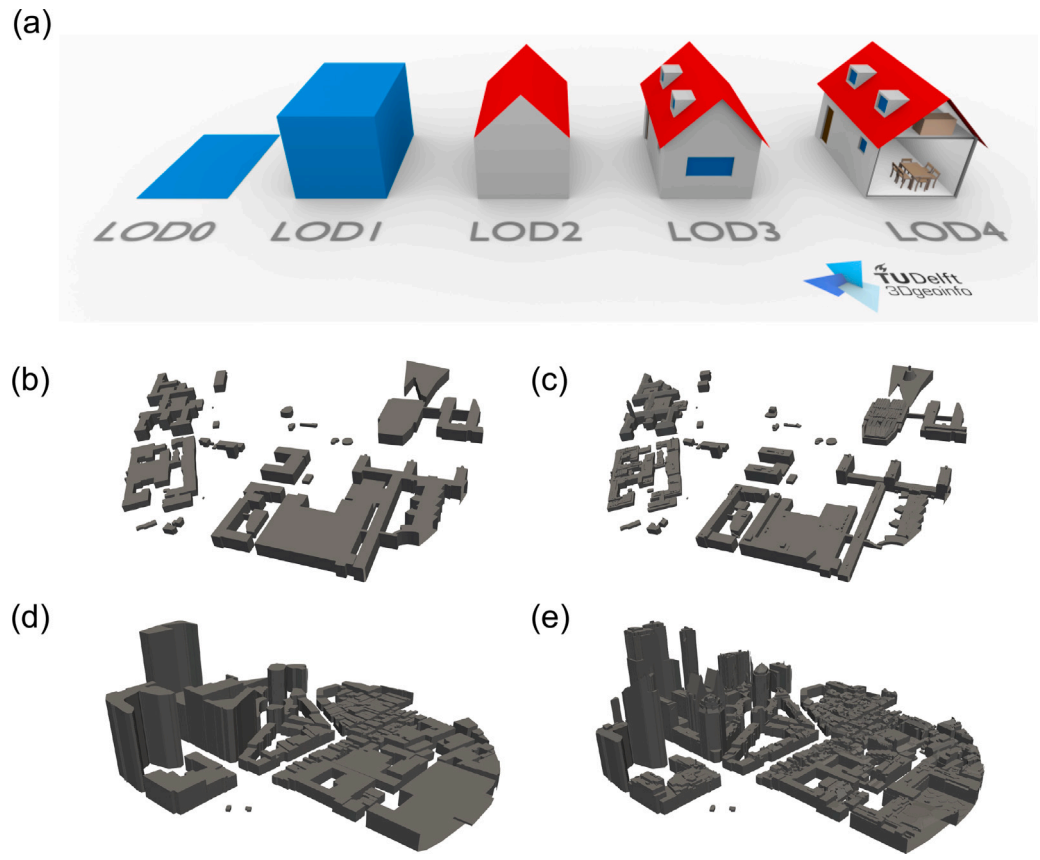

Fig. 1. (a) Consistent geometric definition through the level of detail for urban built environment schematic adapted from Biljecki et al. (2016). The primary difference between LoD 1.x and LoD 2.x is that the latter supports multiple heights in the same building footprint, while the former does not. (b–e) Comparison of part of the geometry illustrating the systematic geometric differences for each city, where the panels on the left (i.e., b and d) show LoD 1.2 while panels on the right (i.e., c and e) show the same region in LoD 2.2.

where $C_{\mu} = 0.09$ constitutes the model coefficient.

The governing equations are discretised in space using a second-order accurate, collocated finite-volume method, while the pseudo-time stepping is used through the Semi-Implicit Method for Pressure Linked Equations (SIMPLE) algorithm to integrate the steady-state equations (Patankar, 1980). All the terms in the governing equations are discretised using blended second-order accurate schemes. Specifically, the gradient terms are discretised using the `cellLimited Gauss linear 1` scheme, which corresponds to a second-order accurate central differencing scheme with a gradient limiter such that the cell face values when extrapolated from the cell centre values remain bounded conditioned on the neighbouring cells. The advective acceleration terms are discretised using the `bounded Gauss linearUpwindV limited` scheme, which corresponds to an upwind biased second order accurate scheme for vector fields (i.e., velocity) with a gradient limiter as used for the gradient terms. The scalar divergence terms are discretised using the `bounded Gauss limitedLinear 1` scheme, which corresponds to a second-order accurate bounded convective scheme, and the viscous diffusion term is discretised using the `Gauss linear` scheme, which corresponds to a second-order accurate central differences. The governing equations are solved using the MPI-parallelised computational toolbox OpenFOAM (version 7) (Weller, Tabor, Jasak, & Fureby, 1998). The steady-state solutions are integrated for a total of 3500 iterations until the normalised residuals plateau for the pressure solver at around 10^{-3}, and those for velocity and the two scalars reach $\sim 10^{-5}$ (Blocken, 2015). All the simulations are run using the Delft Blue super-computing centre (Delft High Performance Computing Centre (DHPC), 2024) at the Delft University of Technology, Delft, using Intel Xeon E5-6448Y CPUs with 64 cores. Each simulation takes approximately 288 CPU hours to obtain converged solutions, requiring approximately 68 GiB of memory and generating a maximum of 5 GiB of data containing the 3D snapshots for velocity, pressure, turbulent kinetic energy, turbulent kinetic energy dissipation rate, and the turbulent viscosity, respectively.

2.2. Mesh design and grid convergence

To simulate flow around a realistic urban area, we choose the Delft University of Technology campus (henceforth TUD-campus) and the city of Den Haag (henceforth the Hague) as representative urban areas in terms of the built environment as they showcase a variety of buildings, vegetation, water bodies, and other semantic surfaces that are located in a single area. Specifically, buildings and semantic surfaces within a radius of 1 km are considered as the region of interest for the simulations, while for the TUD-campus case, only the central university campus is considered. The proximity of the two urban areas to a wind measurement station allows for leveraging incident wind conditions that can be used as boundary conditions for setting up the model. Fig. 2 depicts the choice of the urban area and the computational mesh as discretised in the numerical framework used in this study. The building geometry for LoD 2.2 is obtained from the 3DBAG database (Peters, Dukai, Vitalis, van Liempt, & Stoter, 2022) while LoD 1.2 buildings are directly reconstructed using City4CFD (Pađen, García-Sánchez, & Ledoux, 2022; Pađen, Peters, García-Sánchez, & Ledoux, 2024). Surface features such as terrain, vegetation, and water polygons are obtained from the Dutch National Digital Repository of Geospatial Data (Georegister, 2025). These two tools allow for seamless integration of the building environment into the computational mesh in an automated workflow, ensuring that all the semantic surfaces, such as terrain, water, and vegetation, can be correctly incorporated along

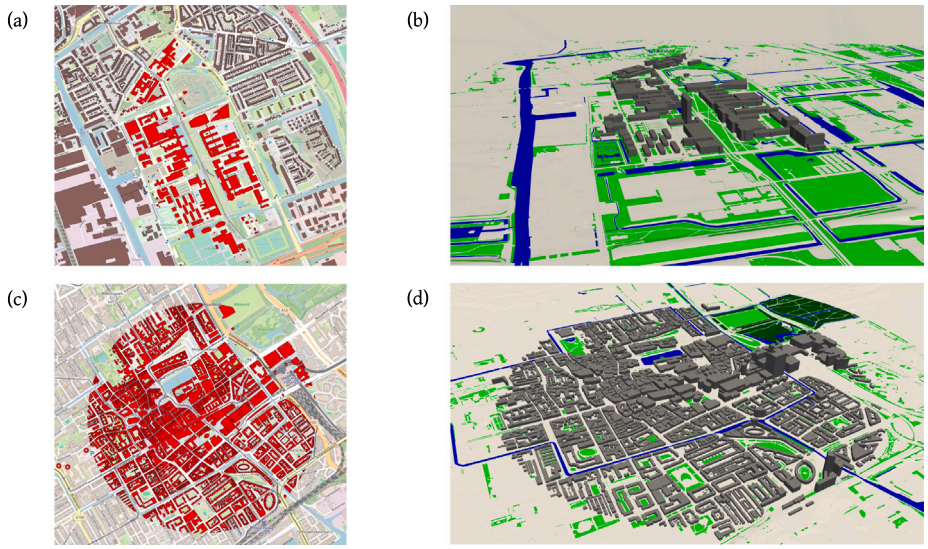

Fig. 2. (a) and (c) Map of the region of interest relative to the other features with the red polygons indicating the built environment that is considered in this study. Figure courtesy of Open Street Map (OpenStreetMap contributors, 2017). (b) and (d) Computational mesh (LoD 1.2) depicting the buildings and the terrain used in the study to simulate the urban environment. Buildings are marked by grey, vegetation is marked by green, forest is dark green, ground/terrain is marked by white, and water is marked by blue.

with the buildings in the region of interest. The total time required for the reconstruction process was 2 h, where data acquisition required 1.95 h, while the reconstruction process required only $\mathcal{O}(100)$ s. Fig. 2(b) and (d) show that the buildings are accurately placed along with the other surfaces, thus improving the representation of the various elements present in the urban environment.

The flow domain is designed following the best practice guidelines as detailed in Blocken (2015) and Franke, Hellsten, Schlunzen, and Carissimo (2011) using a cylindrical domain around the region of interest (ROI) as shown in Fig. 2. The simulation domain consists of the region of interest around which the domain is extended (see Fig. 3). The computational mesh is generated such that closer to the ROI, the mesh is sufficiently fine to resolve the geometric features and is successively refined away from the buildings, as shown in Fig. 3(b). The cylindrical domain enables running various inflow wind directions without meshing the domain for every wind incidence angle, and instead, only the inflow angle is changed in the boundary conditions.

In order to correctly generate the mesh using `snappyHexMesh` application, the underlying background mesh is refined using a hierarchy of relatively refined boxes with level 1 and level 2 refinement as shown in Fig. 3(b). Here, level 1 corresponds to the background grid being halved, while level 2 corresponds to the background grid refined by a factor of 4, respectively. In addition to these refinement regions, to accurately resolve the building surfaces, distance-based refinement is used such that all distances within the first 4 m normal to the building surface are refined with level 5 (i.e., undergo grid refinement by a factor of $2^5 = 32$), and the next 8 m normal to the building surface are refined with level 4 (factor of 2^4 reduction), and the next 13 m normal to the building surface are refined with level 3, respectively. A similar distance-based grid refinement is employed for the terrain, such that the first 3 m are refined with level 5 grid refinement.

To carry out the grid convergence/sensitivity test, we use the TUD-campus case with a wind incidence angle of $\theta = 210°$ with respect to North. A similar grid convergence test was carried out for the Hague case, but it has not been detailed here for brevity. Table 1 details the three meshes considered in the grid convergence test, where the representative grid size is the average grid size computed as

$$\Delta h_r = \left(\overline{\Delta V}\right)^{1/3}, \tag{6}$$

where $\overline{\Delta V}$ is the average cell volume in the domain. As the flow field around the urban area is relatively complex, to avoid contamination of grid sensitivity estimates due to local grid effects, we sample approximately 200 probes and 100 line probes as shown in Fig. 4 within the domain and use the median grid convergence index (GCI) parameter (Celik, Ghia, Roache, & Freitas, 2008) to estimate the suitability and grid independence for this case.

Table 1
Description of the three grids used to understand the sensitivity of the mesh to the predicted results.

Mesh name	Number of cells ($\times 10^6$)	Representative grid size Δh_r (m)
Coarse	9.6	12.46
Nominal	22.35	8.92
Fine	46.61	7.22

Table 2
Grid convergence indicators for the three meshes used to test the sensitivity of the grid on the results predicted. Since the turbulent eddy viscosity (ν_t) is a derived parameter, it has not been included in the table above.

Convergence parameter	$\overline{u}_1$	$\overline{u}_2$	$\overline{u}_3$	$\overline{p}$	k	ϵ
Apparent order	4.4	4.4	4.1	4.7	3.0	4.6
Relative error (%)	0.18	0.15	2.1	1.42	0.61	1.0
Extrapolation error (%)	0.14	0.13	1.94	0.90	0.90	0.70
GCI (%)	0.18	0.17	2.44	1.12	1.13	0.85

As shown in Fig. 4, there is very little difference observed between the velocity profiles across all the mesh sizes, and this is consistent for the other 96 line probes sampled (not shown here) in the comparison. Some differences were observed in the lower portions of the velocity profiles. However, the differences were insignificant, and there was monotonic convergence towards the fine mesh results. Table 2 compares the statistical median values of the grid convergence parameters used in this study. The median apparent order of convergence is higher than the discretisation order of convergence due to similar results obtained on all three meshes. The rest of the three parameters are all below 3% and suggest that the results obtained are sufficiently grid-independent. As a result, the nominal mesh will be used for all the results discussed in the following section as it is sufficiently accurate and computationally efficient based on the metrics presented in Table 2.

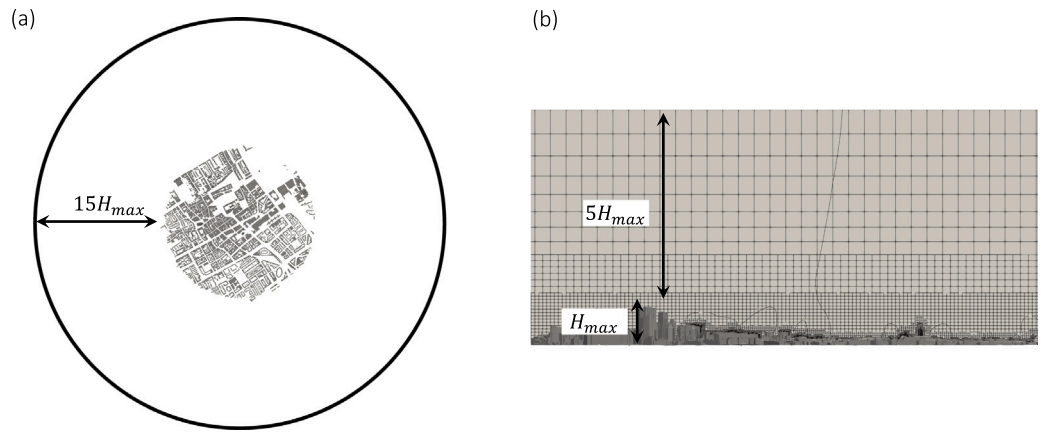

Fig. 3. (a) Top view of the computational domain with the region of interest (ROI) marked by the grey buildings (Franke et al., 2011). (b) Side view of the computational domain with the black solid lines marking the computational mesh and grey colour denoting the buildings.

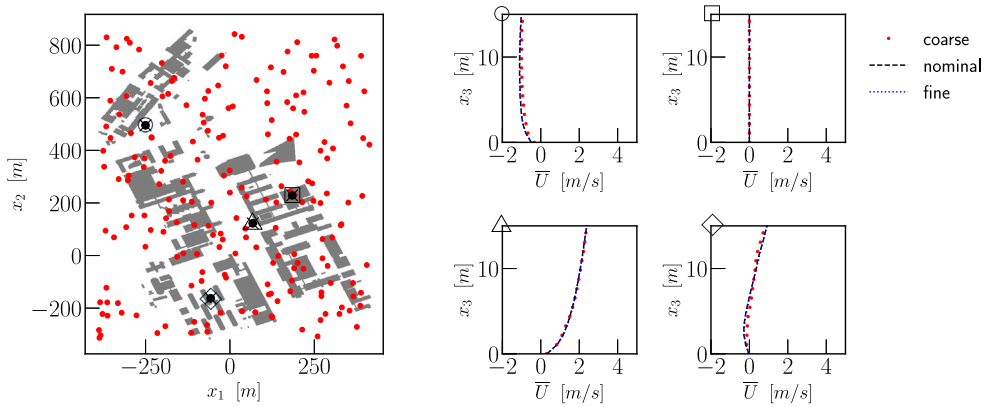

Fig. 4. Top view of the buildings marked in grey, and the vertical line sampling probe locations are marked in red. Four panels on the right compare the velocity profiles at various locations corresponding to the symbol marked at the top left corner of each sub-panel.

Since the flow conditions for LoD 2.2 are identical to those considered for LoD 1.2, the mesh design for LoD 2.2 is based on the geometric resolution requirements. As the building features for LoD 2.2 are relatively more complex when compared to those of LoD 1.2 (Biljecki et al., 2016), a finer grid resolution is required for LoD 2.2 to resolve these small geometric details. Consequently, for LoD 2.2, the computational grid has approximately 48 Million cells. Similar differences between the two LoDs were observed for the Hague case, where LoD 2.2 required a finer grid resolution than LoD 1.2. Effectively, this requires an additional computational cost of 1.5 times for the LoD 1.2 cases. It is also important to remark that this increased cost is expected to be non-linear and is sensitive to the computational framework used and its weak-scaling behaviour; since OpenFOAM scales approximately linearly for the problem sizes considered in this work, there are no substantial parallelisation costs associated when comparing LoD 1.2 and LoD 2.2 for the hardware on which these simulations are run.

2.3. Wind characteristics and boundary conditions

To characterise the wind conditions for the TUD-campus case, we use the weather station data collected by the Delft University of Technology accessed through the weather data platform (https://weather.tudelft.nl/). Specifically, we use the Delfshaven weather station to characterise the wind data to supply the simulation boundary conditions in this paper. As for the Hague case, data from the KNMI data portal (https://www.knmi.nl/nederland-nu/klimatologie/daggegevens) was processed for the Voorschoten weather station. Fig. 5 shows the normalised wind rose for both weather stations over the period from 2002 to 2022. Panel (a) shows the normalised wind rose for the Delfshaven stations with a 1° resolution. For the TUD-campus, most of the incident wind comes from the west, while for the Hague case, most of the incident wind originates in the south (not shown here). The wind histogram shown in Fig. 5(b) follows a log-normal distribution marked by the solid black line. Since we are interested in understanding the average/mean wind conditions in this study, the black dotted line with an x marks the wind speed location chosen as the simulation's representative inflow boundary condition. For the Hague case, the same wind condition corresponds to the mean wind conditions. However, it is important to realise that the KNMI data is measured at 10 m above the ground. At the same time, the Delfshaven measurement station is located approximately 4 m above the ground, thus explaining the difference between the two stations. In our simulations, we consider the 10 m reference velocity at the inflow boundary condition, which corresponds to the 5.0 m/s choice made for the simulations. In this study, fixed increments of 1° are made for the inflow angle to span the entire wind-rose over 360°; consequently, only the wind direction is changed while the inflow velocity magnitude is fixed as detailed below. It is important to note that the flow Reynolds number is large and can be safely assumed to be in the asymptotic range, such that a reference velocity larger than the one prescribed in this case can be linearly applied without loss of generality (Hågbo & Giljarhus, 2024).

At the inlet boundary, the neutral atmospheric boundary layer velocity, turbulent kinetic energy, and turbulent kinetic energy dissipation rate profiles are applied using the log-law equation given by ($\overline{u}_2 = \overline{u}_3 = 0$)

$$\overline{u}_1 = \frac{u_\tau}{\kappa} \ln\left(\frac{z - d + z_0}{z_0}\right), \tag{7}$$

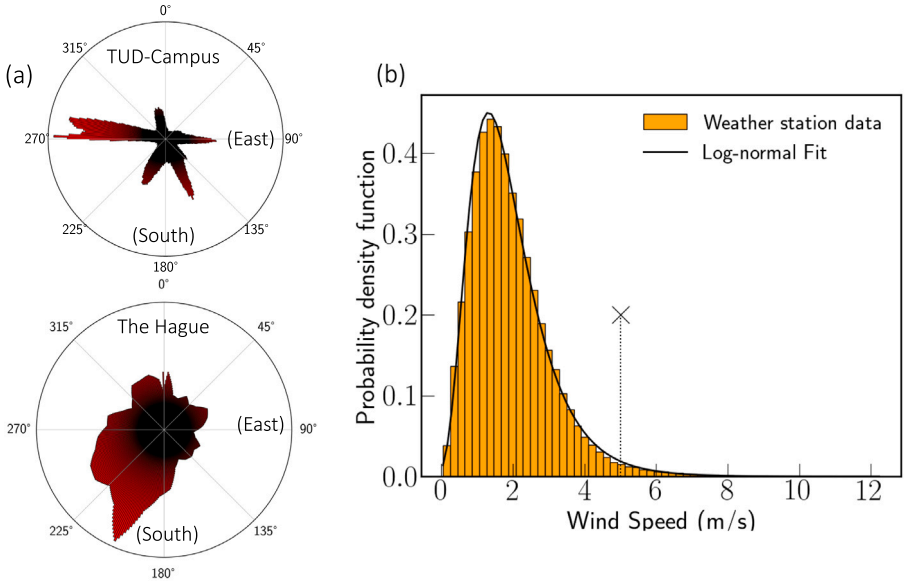

Fig. 5. (a) Twenty-year averaged (2002 to 2022) and normalised wind-rose diagram for Delfshaven Wind-speed probability density function (PDF) for Delfshaven measurement station (top) and Voorschoten measurement station (bottom). The Delfshaven measurement station is used for the TUD-campus case, while the Voorschoten measurement station is used for the Hague case. The radial axis represents the wind incidence angle, with 0 corresponding to the North direction and increasing in angles in the clockwise direction. (b) The fitted log-normal distribution is marked using the black solid line. The vertical black dashed line and cross mark the inflow velocity chosen for the simulations. The wind rose for the Hague weather station is not shown here for brevity.

$$k = \frac{u_\tau^2}{\sqrt{C_\mu}} \sqrt{C_1 \ln\left(\frac{z-d+z_0}{z_0}\right) + C_2}, \tag{8}$$

$$\epsilon = \frac{u_\tau^3}{\kappa(z-d+z_0)} \sqrt{C_1 \ln\left(\frac{z-d+z_0}{z_0}\right) + C_2}, \tag{9}$$

where $u_\tau = \kappa U_{ref} / \ln(\frac{z_{ref}+z_0}{z_0})$ is the friction velocity, U_{ref} is the reference velocity used at $z_{ref} = 10$ m above the ground, $z_0 = 0.5$ m is the aerodynamic roughness length, $\kappa = 0.41$ is the von Kármán constant, d is the displacement height for large roughness elements such as tree canopies, forests, shrubs, etc. and is not used for buildings, $C_1 = 1.44$, $C_2 = 1.92$, and $C_\mu = 0.09$ are model constants. Here, u_1 is aligned along the wind incidence direction and is practically implemented by using a vector sum between the horizontal velocity components that result in the desired velocity magnitude specified at the inlet boundary. As seen in Fig. 2, the various semantic surfaces such as terrain, vegetation, forest, are not explicitly modelled, but are assigned the appropriate aerodynamic roughness length (z_0) based on the updated Davenport classification (Davenport, 1960; Wieringa, 1992) to correctly model the influence of varying terrain features (Davenport, 1960; Shirzadi, Tominaga, & Mirzaei, 2020; Wieringa, 1992). While many other studies have investigated the impact of including vegetation explicitly (Fu, Pađen, & García-Sánchez, 2024; Hui, Tang, Yang, & Mochida, 2024), the focus in this work is to isolate the impact of varying LoD on the flow within the urban built environment without introducing other parameters. Consequently, the vegetation, forest, and terrain features are modelled implicitly through the aerodynamic roughness values of 0.03, 0.8, and 0.5, respectively (Davenport, 1960; Wieringa, 1992). In addition to the above-mentioned u_1, k, and ϵ profiles at the inlet, we use an atmospheric boundary layer wall function at all terrain features such that there is no spurious decrease in the velocity magnitude and shape as it develops within the computational domain (Parente, Gorlé, van Beeck, & Benocci, 2011).

2.4. Suitability of the computational model

In order to accurately and efficiently model the wind flow around complex urban built environments, certain modelling choices have been made, as detailed in the discussion above. In this work, a total of 4 scenarios were simulated as detailed in Table 3, resulting in a total of 1440 simulations that each take 4.5 wall clock hours using 64 CPUs (288 CPU hours) as detailed earlier. While other studies have used a relatively lower wind-incidence angular resolution using increments of 10° (Hagbo & Giljarhus, 2022), in our work, we make use of a much finer angular resolution of 1° to adequately capture the impact of each of the wind directions when calculating the UAV risk as detailed in the following sections. Additionally, the dataset generated in this work can be used for further studies, given the relatively high-resolution wind direction data. While higher-fidelity computational frameworks exist, such as the Large-Eddy Simulations (LES) (Bou-Zeid, Overney, Rogers, & Parlange, 2009; García-Sánchez, van Beeck, & Gorlé, 2018), the computational cost associated with such a framework is significantly higher when compared to the RANS framework detailed in the section above. For example, García-Sánchez et al. note that one realisation for a comparable urban built environment using the LES framework required a total of 340000 CPU hours (in 2018). In contrast, all the simulations detailed in Table 3 required a total of 414720 CPU hours, effectively justifying the choice of the computational approach used in this work. Moreover, most LES frameworks employ a Cartesian grid structure coupled with an immersed boundary method (IBM) to include solid objects such as buildings and trees (Peskin, 2002). This effectively limits the grid resolution, which further limits the geometric resolution that can be used for complex urban built environments. Consequently, despite the numerical and scale-resolving capabilities of the existing LES frameworks, RANS modelling is much more suited to predicting mean wind flow conditions and provides a scalable alternative. It is also important to mention that this modelling framework has been extensively validated and tested for wind tunnel and in-situ mean wind conditions with sufficient accuracy (García-Sánchez et al., 2018; García-Sánchez, Philips, & Gorlé, 2014; Hertwig, Efthimiou, Bartzis, & Leitl, 2012; Moonen, Dorer, & Carmeliet, 2011; Salim, Buccolieri, Chan, & Di Sabatino, 2011, to list a few).

Table 3
List of simulations carried out per scenario, including the two cities and two LoDs with a wind-incidence resolution of 1°.

Case name	LoD	Wind simulations
TUD-Campus	1.2	360
TUD-Campus	2.2	360
The Hague	1.2	360
The Hague	2.2	360
	Total simulations	1440

3. Results and discussions

3.1. TUD-campus case

We start by first presenting the wind-rose weighted average quantity defined as

$$\overline{f}_a = \frac{1}{N_\theta} \sum_{i=1}^{i=N_\theta} w_i |f_i|, \tag{10}$$

where N_θ are the number of wind-incidence angles simulated (in this case 360), w_i is the weight which is the value of the wind-rose pdf for angle θ_i (see Fig. 5), and $|f_i|$ is the L_2-norm if f is a vector quantity or the scalar magnitude when f is a scalar at a given grid-point. The wind-rose PDF is obtained from the weather station data by normalising the wind direction probability at a specific angle such that the area under the histogram is unity. In what follows, we assume LoD 2.2 as the ground truth, as illustrated by the relatively better geometric representation of the built environment in Fig. 1. Fig. 6 shows the non-dimensional $\overline{U}_a$ comparison at three different vertical heights for the two LoDs considered in this study (i.e., LoD 1.2 and LoD 2.2). The average wind flow around the campus exhibits a relatively strong accelerating/funnelling flow commonly observed within the central part of the campus, marked by the white dashed circle (YouTube, 2023). Additionally, both LoDs are able to sufficiently capture the average flow features, where the hot spot for large wind speed in the central canyon between the campuses is relatively underpredicted by LoD 1.2 when compared to LoD 2.2. The LoD 2.2 case, where the tall building is located in the vicinity of the central canyon (white dashed line on the top left panel), exhibits a characteristic difference in its dimensions when compared to the LoD 1.2 scenario. The region with a significant value of $\overline{U}_a$ is observed to be offset away from the adjacent buildings and towards the south-east quadrant in the figure. Since LoD 1.2 attributes a uniform height of the building to the entire footprint, the flow is strained in the lateral direction, leading to a large wind velocity for the LoD 2.2 scenario. Comparing the two LoDs, it is clear that there is a substantial difference between the peak wind prediction, while both LoDs adequately capture the average trend in the flow field.

Despite these differences observed in LoD 1.2 compared to LoD 2.2, as shown in Fig. 6, the regions of high-wind speed are adequately addressed. Additionally, it must be stressed that for this specific case, there appears to be an under-prediction (10%–20% magnitude) of the region of high-wind speed in the LoD 1.2 case. On the west side of the region of interest, systematic differences are observed where LoD 2.2 exhibits relatively higher average velocity when compared to LoD 1.2. However, any generalisation about a direct comparison between LoD 1.2 and LoD 2.2 cannot be translated to a different case, as this is case-sensitive, as detailed later. While the magnitude is not substantially different between the two LoDs, the spatial extent of the high-speed regions is demonstrably distinct between the two LoDs, with a relatively greater extent predicted by LoD 1.2 than LoD 2.2. Thus, we first note that the overall trend for this case suggests that the wind-rose weighted average wind speed is observed to be sensitive to the difference in the LoDs.

For safe UAV operations, knowing the locations of high-wind speed is not sufficient as it does not provide a valuable metric for other unsteady processes that may be present; this is especially true for a steady-state RANS simulation where such unsteady features are absent by definition as detailed in Eq. (1). Consequently, to understand the risk associated with UAV operations, a probabilistic framework must be considered where the high-wind speed regions conditioned on large TKE regions can be used to create a risk map as a function of space. Additionally, looking at the velocity or the TKE levels independently can result in diverging conclusions. This metric is motivated by different-sized UAVs interacting differently with the flow around them. The term risk here is used in the broadest sense and can be referenced as predicted risk potential. To this end, we consider the risk map, which is defined as the probability given by

$$\mathcal{P}^r \equiv \mathcal{P}\left(U^* > \alpha \cap k^* > \beta\right) \tag{11}$$

where $\mathcal{P}^r$ is the joint probability that the non-dimensional velocity $U^* \equiv U/U_\infty$ exceeds a given value α and the non-dimensional TKE $k^* \equiv k/U_\infty^2$ exceeds a value β, where both α and β are defined constants. These constants are functions of the urban morphology and require an understanding of how the flow is expected to respond to a given urban morphology. For example, for heterogeneous urban areas, the flow within the urban canopy is expected to have relatively larger energy dissipation and thus lower levels of U^* and k^* and vice versa for non-heterogeneous urban areas. Additionally, since different-sized UAVs interact with the flow around them differently, α and β can be set based on the UAV characteristics and expected flow levels, as discussed earlier. We also carried out a systematic sensitivity analysis for the threshold values of α and β to better quantify the impact of choosing specific thresholds. Specifically, we considered $\alpha = [0.1 - 0.7]$ and $\beta = [0.03 - 0.1]$ with $\delta_\alpha = 0.1$ and $\delta_\beta = 0.01$ being the increments for each parameter, resulting in a total of 56 different combinations of the exceedance parameters to better understand the behaviour of the risk map subject to the two parameters. A few combinations of α and β are detailed in Appendix, which suggests that for small values of α, it is difficult to draw precise conclusions as the entire area of interest is classified as a high-risk region, which is not surprising. While cases with increasing values of α, LoD 1.2, are observed to be consistently under-predicting the risk region. For a detailed discussion, the readers are referred to Appendix. Currently, there is no standard that exists, but it is often reported through the manufacturer of the UAV as a maximum wind resistance rating (DJI, 2025; Gao et al., 2021). Consequently, in our case, unless otherwise specified, we use $\alpha = 0.4$ and $\beta = 0.08$ for all the discussion relating to the risk map $\mathcal{P}^r$. In Eq. (11), the risk map can be identically defined through a union operator, which would yield a relatively larger risk region for the same values of α and β. The choice of the intersection operator was motivated by the need to have a relatively less conservative framework, as that would provide a more viable path for trajectory optimisation within urban environments. For UAV applications, we consider 7 m and 10 m above the ground as representative heights for wind speed within the urban environment. These two heights are motivated by the need to better understand the risk associated with smaller drones that primarily navigate the urban canopy region.

Fig. 7 shows the risk map comparison for the two LoDs considered in this study. Despite the relatively good comparison for the wind speed in Fig. 6, the risk map clearly highlights some differences when directly comparing the bulk parameters for two different LoDs. In this case, there is quite a large discrepancy observed between LoD 1.2 and LoD 2.2 for $\mathcal{P}^r = 0.5$, which can be interpreted as a 50% chance that both the mean velocity and the TKE levels exceed the threshold's ($\alpha = 0.4$ and $\beta = 0.08$). Large differences are observed in regions with flow separation and canyon-like regions where the mean flow is strained. Since identical turbulence closure and wind incidence conditions are used, these differences can be attributed to the difference in the geometric resolution, i.e., LoD. While the risk map in Fig. 7 is shown in two dimensions, a 3-dimensional risk map (perhaps more aptly a field) can also be estimated, and regions of large $\mathcal{P}^r$ can be

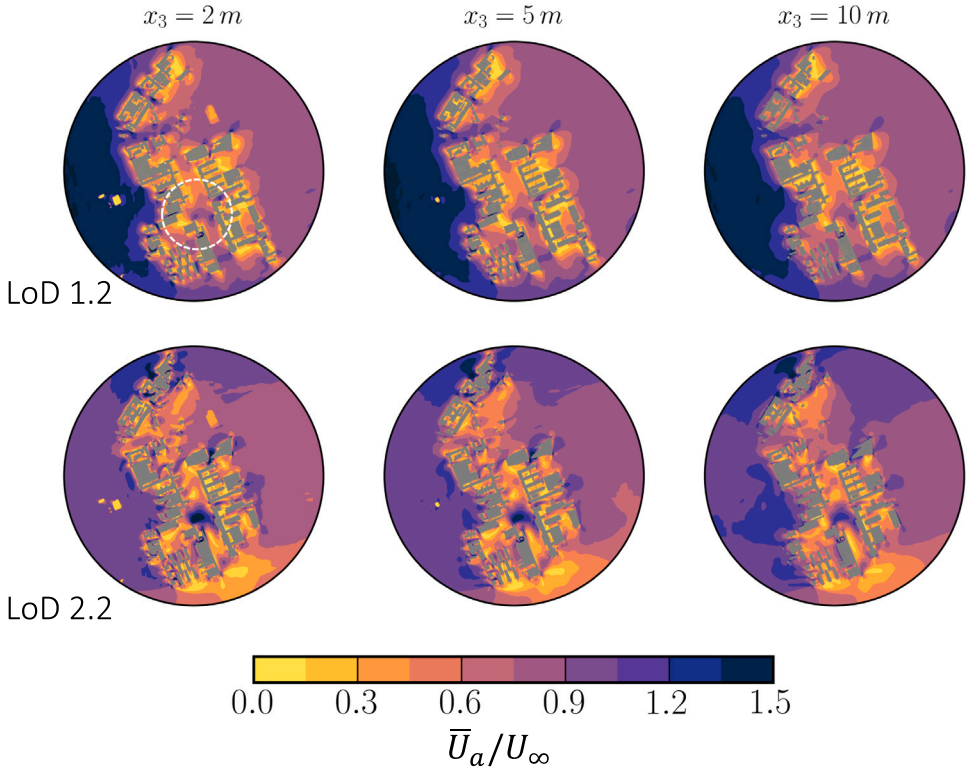

Fig. 6. Top row: Non-dimensional wind-speed for LoD 1.2, where the dark shades mark larger wind-speed while lighter shades mark low wind-speed. Here U_∞ = 5.0 m/s, which is the wind speed at the inflow boundary condition. Bottom row: Same as the top row, except that this row corresponds to building LoD 2.2.

identified to inform UAV trajectory planning and routing. In this case, the region would constitute iso-surfaces as opposed to iso-contours such as the ones shown here; however, for the sake of brevity, the iso-surface for high-risk regions has not been presented. Despite the lack of any unsteady features in the results discussed thus far, the risk map serves as a first indicator which can be used to identify potentially problematic regions where a more informed trajectory decision can be made using unsteady/real-time sensed data.

3.2. The hague case

The area of interest in the Hague case has a substantially different urban morphology when compared to the TUD-campus case. Specifically, the built environment has a traditionally compact arrangement as opposed to the relatively sparse built environment observed in the TUD-campus case. As shown in Fig. 8, in some locations of the region of interest, a consistent over-prediction can be observed for LoD 1.2 compared to LoD 2.2. This over-prediction mainly seems to overestimate the total region that experiences a high wind speed for LoD 1.2 due to its attribution of a single height per footprint polygon (Biljecki et al., 2016). For the x_3 = 2 m slice in panel (a), both the low-speed and high-speed regions are relatively well captured by LoD 1.2 and LoD 2.2. Since pedestrian wind comfort (Sanz-Andres & Cuerva, 2006) is typically evaluated at this height, this would indicate that for this specific urban scenario, the differences between the two LoDs are small, unlike the TUD-campus case. At the same time, most of the differences are observed at the semantic surfaces, such as water and vegetation, between the two LoDs for high-speed regions. This is especially true as the semantic surfaces, along with the x_3-varying terrain surfaces, significantly impact the local wind conditions, thus further demonstrating the vital role these features play within the urban built environment despite the highly parametrised/modelled methodology (Fu et al., 2024). In the city centre, where there is a four-way pedestrian intersection (upper left side of the white dashed line on the top left panel), LoD 1.2 wind predictions are observed to be relatively smaller (5%–10%) when compared to that of LoD 2.2 such that LoD 1.2 predicts a larger extent and more intense high-speed region. A similar observation can be made in the region that is relatively close to the periphery of the city centre (lower right side of the white dashed line on the top left panel), where a similar four-way crossing is located opposite a relatively high-rise building. For all panels with LoD 1.2, a relatively lower wind speed is observed when compared to that for LoD 2.2, suggesting a systematic under-prediction with LoD 1.2. Similar observations can be made for the various x_3 locations and neighbourhoods within the region of interest, suggesting a strong influence of the LoD. These results also indicate the importance of using semantic surfaces to represent the various elements of the urban fabric, such as water, vegetation, and forest, that can be observed to have a large impact on the wind speeds observed in these regions.

For the Hague case, the joint probability exceedance parameters are defined to be $\alpha = 0.4$ and $\beta = 0.05$ and Fig. 9 shows the risk map for this case. Comparing LoD 1.2 against LoD 2.2, there is clear evidence that despite an overall larger mean wind speed prediction in both extent and magnitude, the joint probability of both the wind speed and the turbulence level is consistently under-predicted when using LoD 1.2. This joint probability definition differs from the comfort class categorisation (Lawson, 1978), which is only conditioned on wind speed. It is clear from the trend that the locations of high wind speed are a subset of high turbulence levels based on the fact that the black contour lines are enveloped by the white contour lines in Figs. 7 and 9. The information about high turbulence levels is essential in the case of UAVs, given that the relevant gradients are proportional to the size of the UAV, and this information can be extracted from the turbulence levels. While LoD 1.2 can capture the risk regions (defined in Eq. (11)), there is a systematic under-prediction of the extent and the risk magnitude associated. These under-predictions are systematically located in regions around closed corridors underlying semantic surfaces (see Fig. 2).

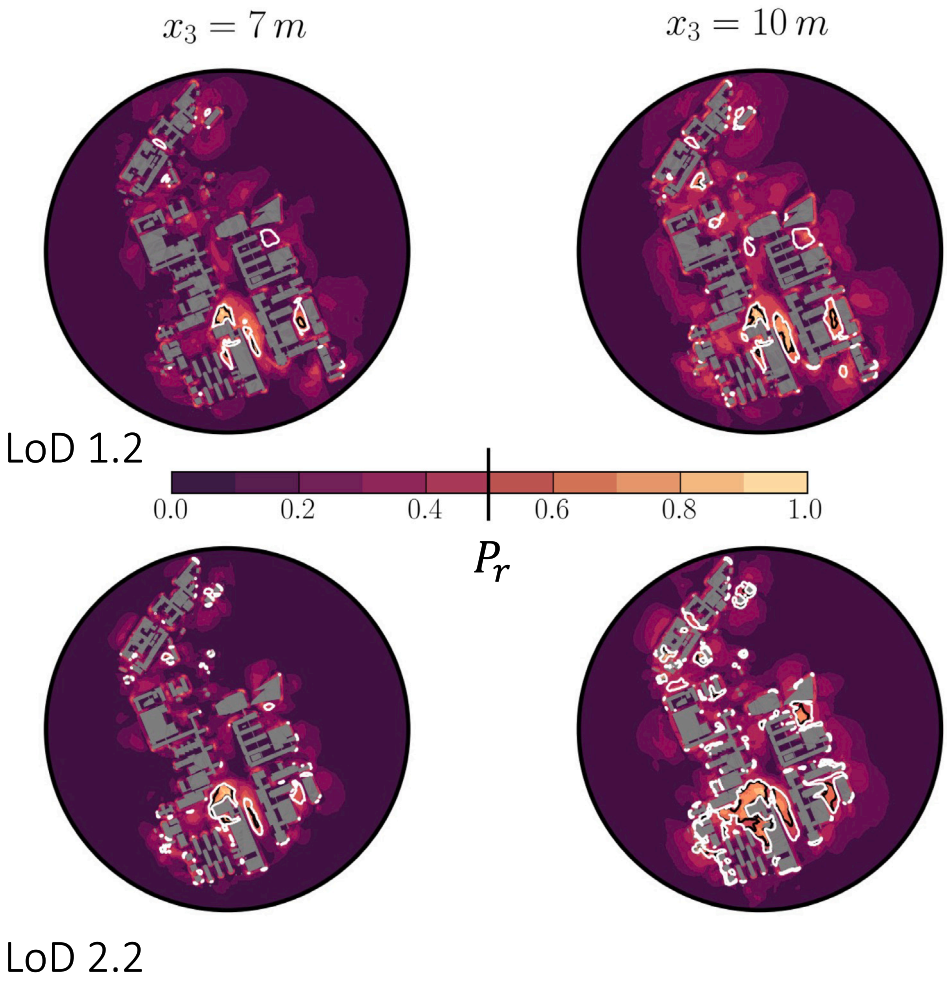

Fig. 7. Comparison of the risk metric as a function of the two LoDs considered in this study at 7 m and 10 m above the ground ($x_3 = 0$). The top row corresponds to LoD 1.2, while the bottom row corresponds to LoD 2.2. Here, the solid black line marks the contour for $\mathcal{P}^r = 0.5$, and the solid white line marks the contour for $\mathcal{P}^r_k = 0.5$, which is the probability that $k^* > \beta$.

Furthermore, comparing the two horizontal slices detailed in Fig. 9, it is clear that further away from the ground (comparing x_3 = 7 m against x_3 = 10 m), the overall region marked by the risk map increases as expected. The densely built environment, in this case, limits the extent of the risk regions to areas such as road crossings, open parks, and the periphery of the region of interest, unlike the TUD-campus case, which is sparsely packed with buildings. This systematic difference between the two areas suggests that urban morphology can play a big role in characterising the viability of UAVs, primarily through the use of the risk map.

In the previous sub-section, most of the discussion focused on illustrating the impact of LoD using a relatively larger domain and the variations therein. However, the differences in LoD can significantly impact the local risk as a consequence of the systematic height and geometry differences between LoD 1.2 and LoD 2.2, as illustrated in Fig. 1. To demonstrate such a local effect, we consider the east corridor of the Hague case as shown in Fig. 10 that compares the risk contextualised with the buildings marked in grey to better understand the differences that arise due to the variation in LoD. In the region marked by the dashed circle, LoD 1.2 attributes a single height to the building footprint as opposed to LoD 2.2, which retains the individual buildings at the east and west sides of the circle. This leads to a funnelling effect when the wind is incident from the north and south directions, leading to a relatively higher risk forecast as a consequence of this acceleration. However, such a marked effect due to the differences in building height is not observed for the same location when considering LoD 1.2, which yields a relatively lower risk in the downstream region of the buildings. In the region marked by the dashed square, a similar effect can be observed where LoD 1.2 fails to correctly capture the differences in the building footprint and instead attributes a single height to the entire footprint, thus leading to a relatively less tall building and lower risk prediction when compared to LoD 2.2. When compared to LoD 2.2 on the south-east corner of the dashed square, the building geometry is drastically different in LoD 1.2. The tower-like structure can lead to relatively large flow separation, thus inducing a downwash leading to large velocity and TKE magnitudes at the four-way crossing. Lastly, the dashed triangle illustrates the importance of including sloping roofs (included in LoD 2.2 but not in LoD 1.2) in addition to the correct building heights that can greatly impact the wind flow within the urban canopy. As seen in this case for the region marked by the dashed triangle, LoD 2.2 predicts a relatively higher risk in the central region when compared to LoD 1.2. While these observations are only shown for a relatively small region of interest for one of the cases, similar observations were made for the TUD-campus case (not shown here) and illustrate the importance of using the right level of detail for wind simulations. These observations collectively indicate that using a probabilistic metric conditioned only on the wind speed can provide a false sense of similarity where the effect of the geometric detail can seem less important when, in reality, substantial differences exist in the data. Since building height constitutes one metric in the urban morphology characterisation (Fleischmann, Romice, & Porta, 2021; Labetski et al., 2023) and the attribution of building

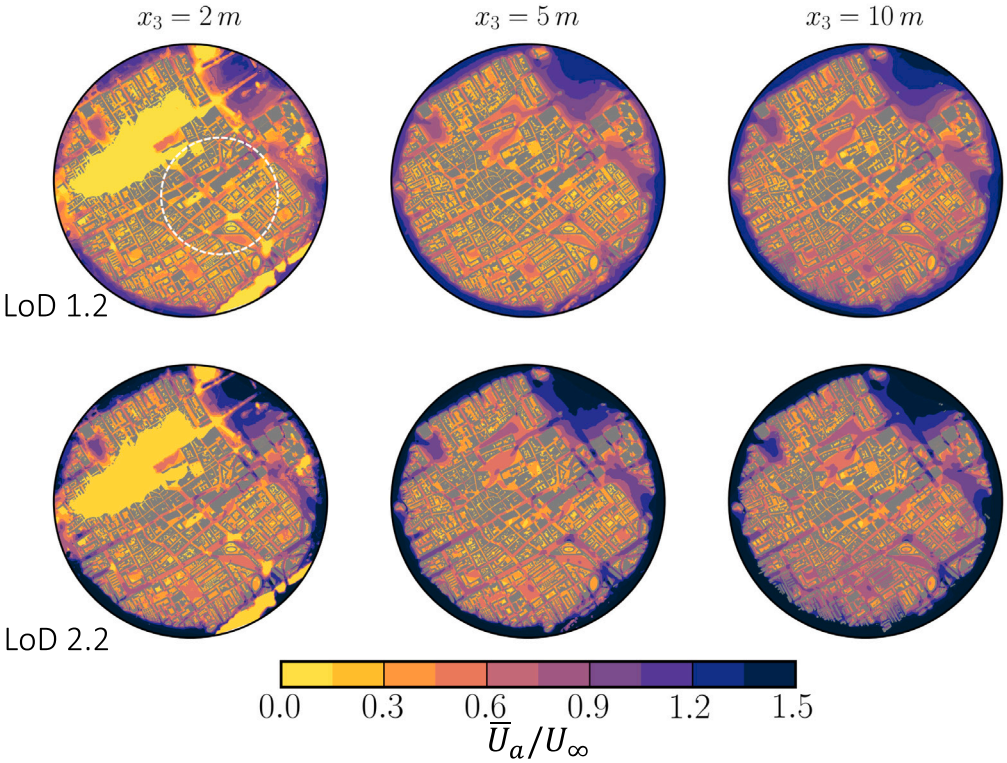

Fig. 8. Top row: Non-dimensional wind-speed for LoD 1.2, where the dark colours mark larger wind-speed while lighter colours mark low wind-speed. Here U_∞ = 5.0 m/s, which is the wind speed at the inflow boundary condition. Bottom row: Same as top row, except that this row corresponds to building LoD 2.2.

height is dependent on the LoD classification (Biljecki et al., 2016; van der Vaart et al., 2024), it is important to correctly isolate the effect of such a systematic building characterisation in urban fluid dynamics applications. Specifically, when using mixed LoD building models, the impact of LoD can become substantially large depending on the parameter of interest, and a generalised conclusion of the effect of such a characterisation should be made with caution.

3.3. Pedestrian wind comfort

As presented in the sections above, comparing the wind-rose weighted velocity ($\overline{U}_a$) and the risk map ($\mathcal{P}_r$) for the two LoDs exhibits a significant difference. While the primary focus of this study is on LoD effects for drone-related wind assessments, pedestrian wind comfort (PWC) serves as a valuable diagnostic for evaluating wind comfort at near-ground level, where the influence of geometric detail is particularly pronounced. Including PWC is relevant not only for general urban wind safety analysis but also for ensuring comfort and safety in areas of potential drone infrastructure, such as vertiports and transit corridors (Federal Aviation Administration, 2024; Muia et al., 2024). As shown in the previous sub-sections, LoD plays a crucial role in capturing flow variations at pedestrian height, making PWC a complementary metric to assess the fidelity and applicability of urban wind simulations. For a more generalised perspective on other wind engineering applications, the Pedestrian Wind Comfort (PWC) is used for safety assessment (NEN, 2006). Specifically, to better understand the impact of LoD on PWC, we use the NEN8100 standard for the wind velocity data at 2m above $x_3 = 0$ in what follows. Table 4 details the NEN8100 PWC criteria used to categorise the various grades of comfort. Using this definition, we compared the effect of LoD on PWC for the two cases detailed in this work to better understand the impact of LoD.

As shown in Figs. 11 and 12, there are distinct differences in the PWC when comparing LoD 1.2 against LoD 2.2. Specifically, LoD 1.2 is observed to consistently under-predict the grade of the PWC when compared to LoD 2.2. It is also pertinent to note that while significant differences are observed for the wind-rose averaged velocity and the risk map, the PWC map fails to capture the finer details despite using identical statistical data. For the TUD-campus case, the PWC map for LoD 1.2 fails to adequately capture grade C in the central part of the region of interest that is famously known for high wind risk (YouTube, 2023). As for the Hague case, a similar overall trend is observed where the grade B PWC is not predicted in the centre of the region of interest by LoD 1.2. Additionally, the areas with relatively higher grades of discomfort in the north-east part of the region of interest are also not correctly predicted by LoD 1.2 when compared to LoD 2.2. It is interesting to note that while some differences are observed in the PWC maps as detailed in Figs. 11 and 12, the differences observed between the two LoDs are not substantially large and are confined to a difference in PWC grade that is consistently one level lower for LoD 1.2 when compared to LoD 2.2. This is not a surprising outcome as the flow 2m above the ground is governed by the near wall effects that are largely governed by the in-canopy heterogeneity (Zhang, Zhu, Yang, & Wan, 2022). Consequently, any differences observed at this height are small unless large building height changes are introduced due to the limitation in LoD 1.2 definition. This is evidenced when comparing the PWC map for the Hague case and the TUD-campus case in the central part of the region of interest, where such effects dominate the flow.

Table 4
Pedestrian wind comfort criteria definition (NEN, 2006) for various activities. The probability mentioned in the first column is taken to be per hour, and the velocity is prescribed in m/s where U_I is the in-situ velocity.

$\mathcal{P}(U_I > 5)$	Grade	Sitting	Strolling	Traversing
<0.025	A	Good	Good	Good
0.025–0.05	B	Moderate	Good	Good
0.05–0.1	C	Poor	Moderate	Good
0.1–0.2	D	Poor	Poor	Moderate
>0.2	E	Poor	Poor	Poor

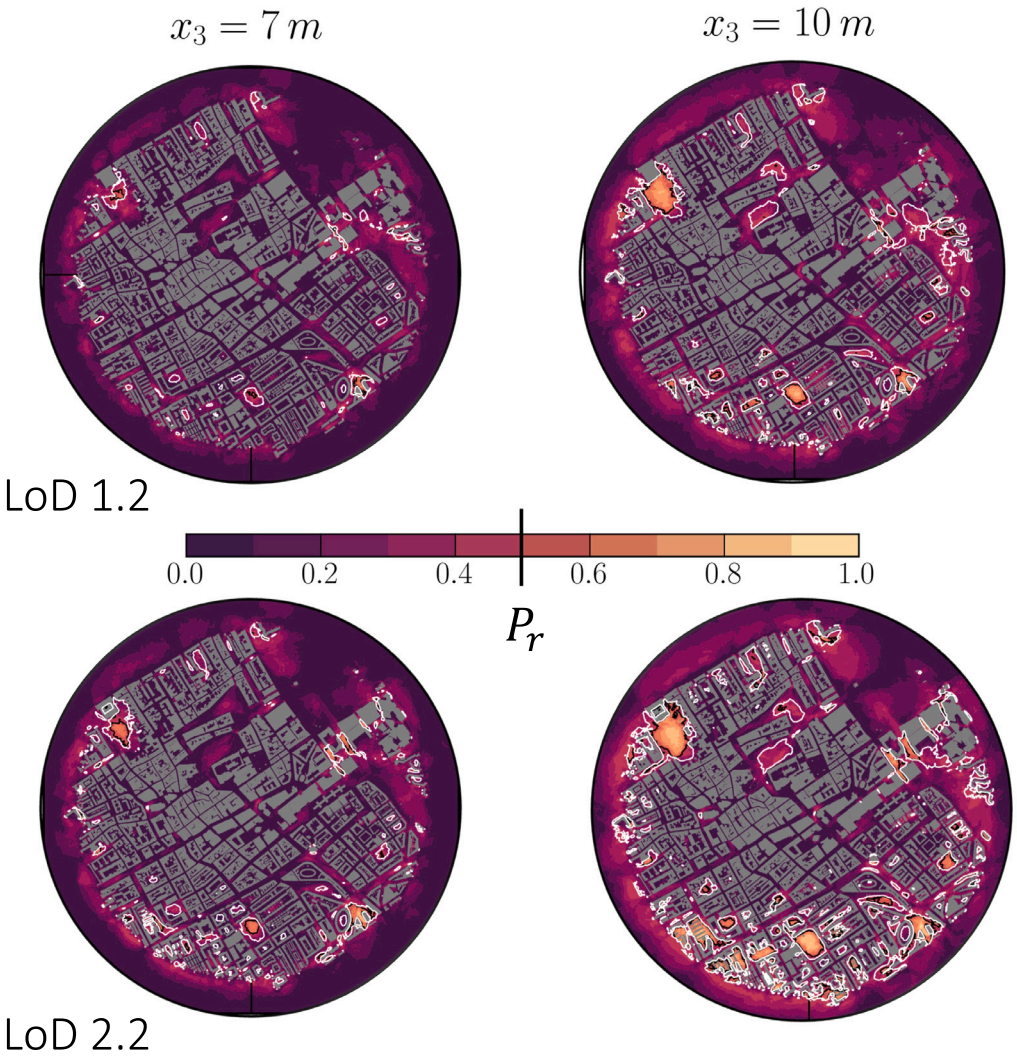

Fig. 9. Comparison of the risk metric as a function of the two LoDs considered in this study at 7 m and 10 m above the ground ($x_3 = 0$). The top row corresponds to LoD 1.2, while the bottom row corresponds to LoD 2.2. Here, the solid black line marks the contour for $\mathcal{P}^r = 0.5$, and the solid white line marks the contour for $\mathcal{P}^r_k = 0.5$, which is the probability that $k^* > \beta \equiv 0.05$.

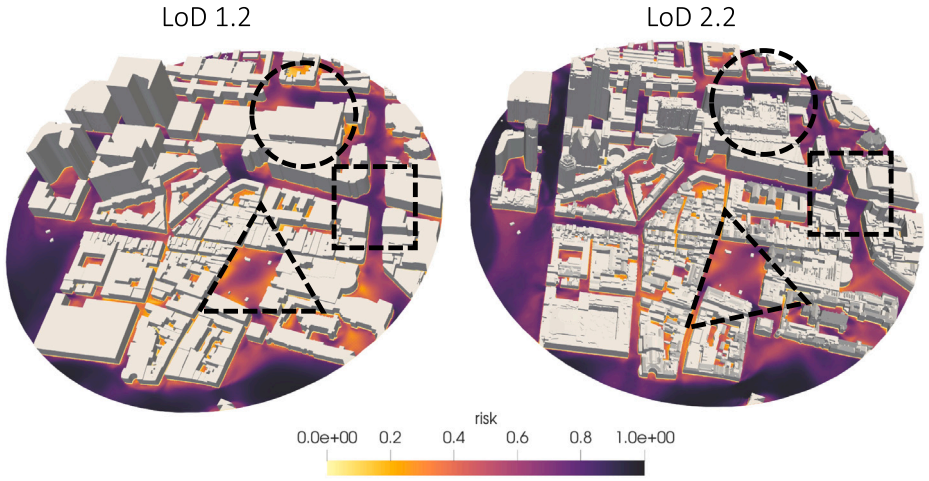

Fig. 10. Comparison of the risk metric as a function of the two LoDs zoomed on the east corridor at 7 m above the ground. The dashed lines mark the various locations of interest, while the colourmap marks the risk, and the solid grey lines mark the buildings at the two LoDs.

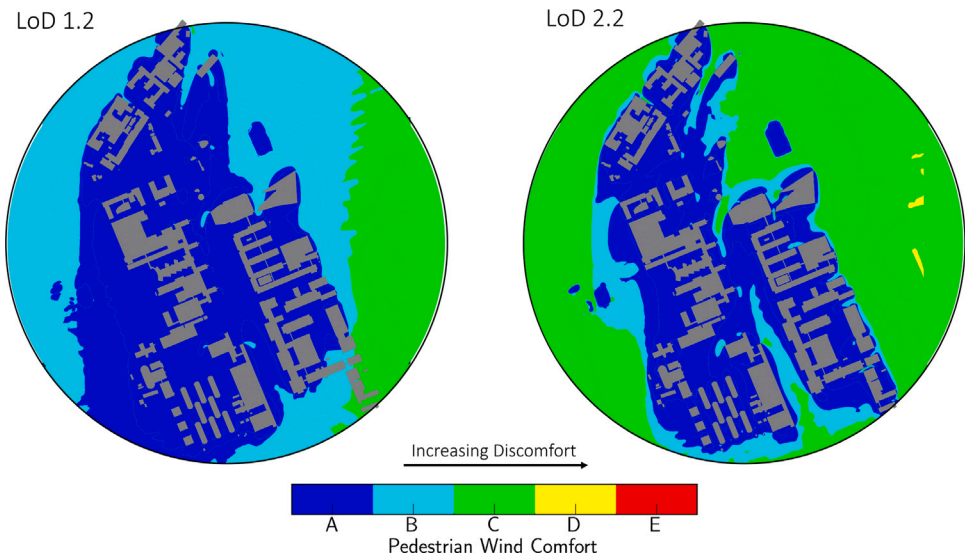

Fig. 11. Comparison of the PWC for the TUD-campus case using 20-year historical data.

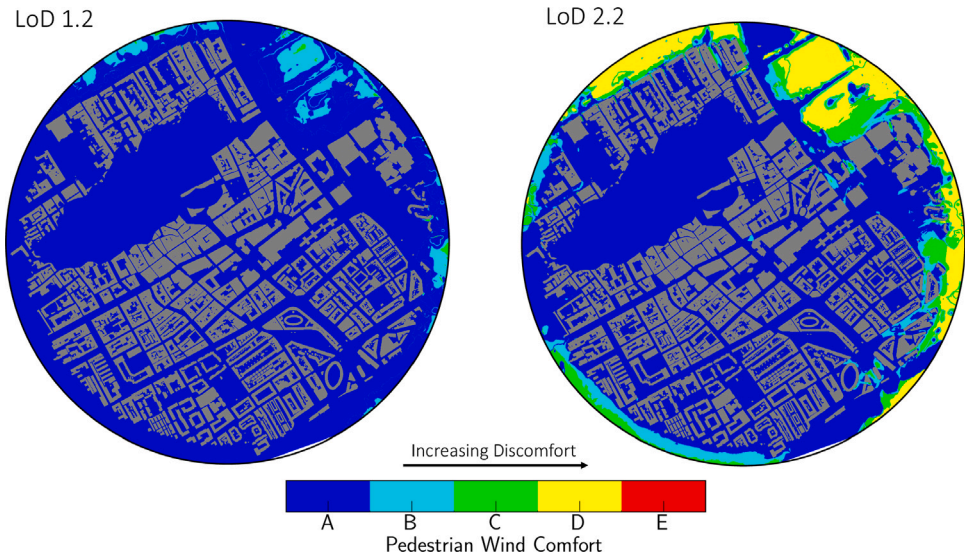

Fig. 12. Comparison of the PWC for The Hague case using 20-year historical data.

Since the risk map is not limited by the height above which it needs to be defined, it does not suffer from the intrinsic assumptions that may limit characterising the differences. In other words, further away from the ground, the differences induced by the LoD can significantly impact the flow; thus, the risk map is a valuable tool for UAV risk predictions.

Overall, these observations suggest a substantial impact of the level of geometric detail on the wind parameters of interest in urban environments. Additionally, it is clear from the above discussion that spanning the large set of parameters using a computational fluid dynamics (CFD) approach is not feasible for producing engineering solutions. This is true even for a turbulence-modelled Reynolds-Averaged Navier–Stokes (RANS) type simulation framework. This makes predicting flows in complex urban areas computationally expensive and has remained a challenge even when it comes to RANS-style simulations subject to varying inflow wind incidence and even more so when relatively higher fidelity computational methods are applied (Nazarian, Krayenhoff, & Martilli, 2020).

4. Conclusions and discussions

In this work, we studied the effect of a systematic method to characterise one of the many urban morphology parameters, i.e., building geometry level of detail, on wind prediction capabilities of the RANS computational approach using a wind-incidence angular resolution of 1°. We found that lower LoD, specifically LoD 1.2, has a tendency to over-predict the wind speed within the urban area when compared to LoD 2.2 due to a single height attributed to the entire footprint in LoD 1.2 in certain locations. The differences between LoD 1.2 and LoD 2.2 overall for the directionally averaged wind speed are not as large (less than 20%) when compared against each other. However, a systematic under-prediction is observed in LoD 1.2 when the joint exceedance probability of velocity and turbulence levels is considered. Given that LoD 1.2 is typically used in urban flow simulations, statistical risk assessment relying on this quantity, such as pedestrian wind comfort, pollutant transport, and other risk metrics, must be made with sufficient caution, as evidenced by the differences observed in the pedestrian

Fig. A.13. Comparison of the risk map for varying values of α and β parameters starting. The black solid lines correspond to LoD 1.2, and the white solid lines correspond to LoD 2.2. The colours mark the risk map associated with LoD 2.2, while the grey region corresponds to LoD 1.2. Top row corresponds to $\alpha = 0.03$ and $\beta = 0.05$, middle row corresponds to $\alpha = 0.04$ and $\beta = 0.06$, while the bottom row corresponds to $\alpha = 0.05$ and $\beta = 0.09$, respectively.

wind comfort maps. Our simulation data also suggests that while wind-rose (i.e., directionally) averaged wind speed predictions may seem relatively consistent across LoD 1.2 and LoD 2.2, a closer look at the statistical flow parameters, such as the risk map as introduced in this work, suggests a consistent under-prediction when using LoD 1.2 for the two test scenarios discussed. Consequently, when presenting annual forecasts and risk metrics for parameters such as wind comfort, mean pollutant dispersion, and other similar statistical flow features, when available, a higher level of geometric detail must be used instead of the conventional LoD 1.2, which can severely under-predict the mean flow parameters.

While our results provide novel insights through the use of the risk map and the systematic characterisation of the LoD for urban wind flow applications, this work is subject to a number of limitations. One of the fundamental limitations of the turbulence-modelled RANS framework is that it inhibits the inclusion of unsteady features in flow dynamics. This is especially true for regions of the flow where the mean wind is observed to separate, inducing a relatively large form drag, where steady-state models like the ones applied in this work have relatively poor predictive capabilities. Additionally, the risk map, as defined in this work, is a first attempt to move away from a mean prediction of the wind flow and arrive at a coherent statistical framework that can be directly applied to a variety of urban wind simulations and their applications. As a result, a relatively generic framework through the definition of α and β is proposed that is agnostic to the target application. This further puts the burden of adequate cut-off values to be defined by the user for their respective application, thus rendering the tuning parameters relatively ambiguous. To alleviate some of the ambiguity, an extensive parameter sensitivity has been conducted in Appendix.

In conclusion, our work systematically investigated the impact of the geometric level of detail in the built environment to aid future

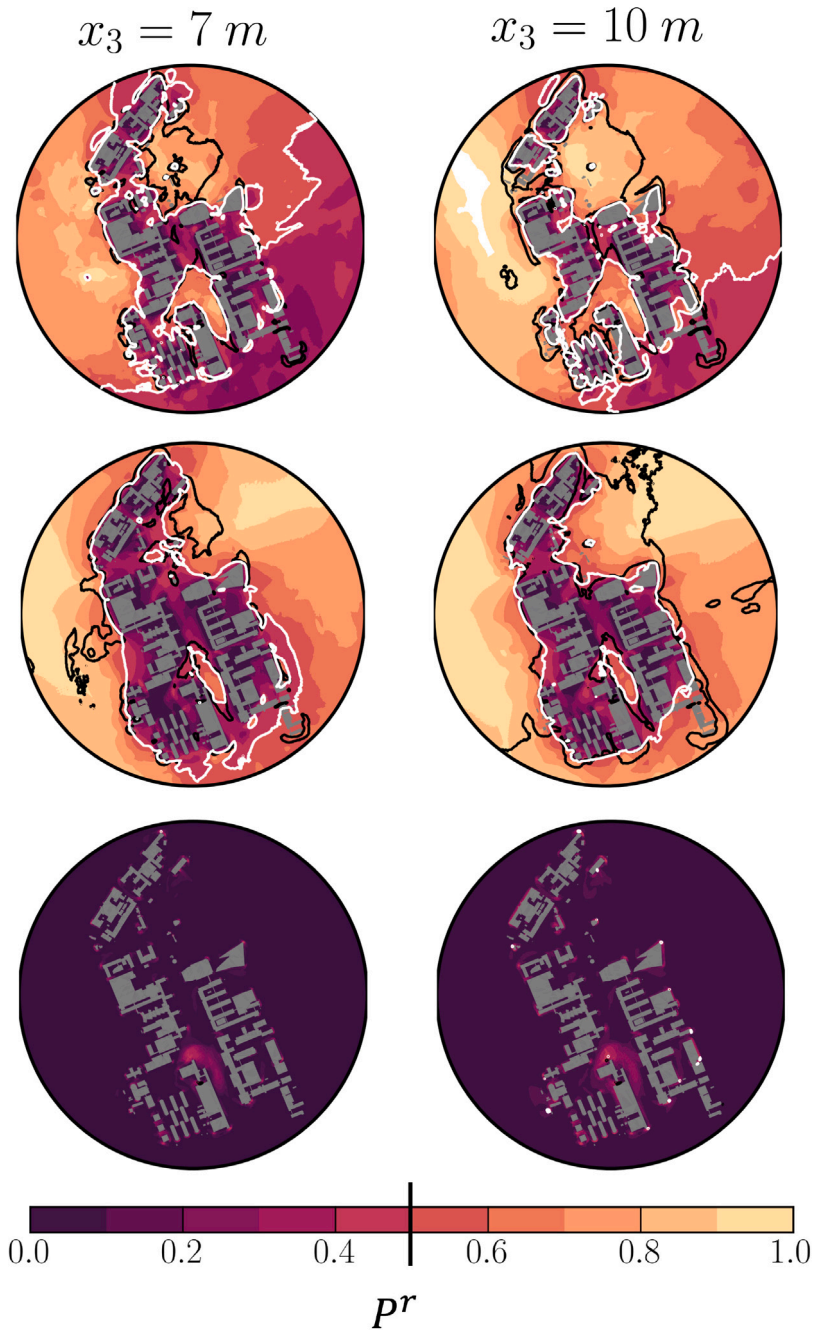

Fig. A.14. Same as Fig. A.13 with the top row corresponds to $\alpha = 0.06$ and $\beta = 0.04$, middle row corresponds to $\alpha = 0.07$ and $\beta = 0.03$, while the bottom row corresponds to $\alpha = 0.07$ and $\beta = 0.09$, respectively.

studies for green technologies, such as replacing UAVs with last-mile transit and proposed the use of a risk map for trajectory planning. Our work provides a novel statistical framework as a first step in urban microclimate modelling applied to UAV trajectory planning and routing using an accurate and computationally efficient simulation framework. Based on our observations and data, we find that any generalisations of the overall urban morphological response to the inflow conditions must be made with care as the transfer function between the input and output is not known *a priori*. This suggests that urban morphology can play a big role in how the risk is distributed over the region of interest, as our data demonstrates. Since the parameters required to characterise urban morphology require many metrics, concluding the universality of a few parameters can be speculative at best, if not entirely problematic. Our data suggest that even small changes in the geometric characterisation of the buildings introduce systematic differences in the risk parameters and mean wind predictions. Thus, universality regarding relatively more complex urban morphological responses requires a detailed investigation and more comprehensive numerical experiments.

CRediT authorship contribution statement

Akshay Patil: Writing – original draft, Visualization, Validation, Software, Methodology, Formal analysis, Data curation, Conceptualization. **Clara García-Sánchez:** Writing – review & editing, Supervision, Resources, Project administration, Methodology, Investigation, Funding acquisition, Formal analysis.

Carbon footprint statement

This work made use of the DelftBlue supercomputer and had an estimated footprint of 1051 kg CO_2-equivalent (at least if not higher) using the Green Algorithms (http://calculator.green-algorithms.org/). The input data used to arrive at these estimates were: Runtime — 6480 h, Number of cores — 64, Xeon E5-2683 v4, and Memory available: 100 GiB located in the Netherlands. This is equivalent to taking 0.65 flight(s) from New York (U.S.) to Melbourne (Australia).

Code availability

All of the code can be found at the public repository Click Here

Funding

This work has received funding from the European Union's HORIZON Research and Innovation Programme, project REFMAP, under Grant Agreement number 101096698. This work was also made possible by the use of computational resources of the DelftBlue supercomputer, provided by the Delft High-Performance Computing Centre (https://www.tudelft.nl/dhpc).

Declaration of Generative AI and AI-assisted technologies in the writing process

During the preparation of this work, the authors used Grammarly in order to proofread and make grammatical corrections. After using this tool/service, the authors reviewed and edited the content as needed and take full responsibility for the content of the publication.

Declaration of competing interest

The authors declare that they have no known competing financial interests or personal relationships that could have appeared to influence the work reported in this paper.

Appendix. Exceedance parameter sensitivity on the risk map

To better quantify the sensitivity of the risk map parameters, we compare the effect of risk map prediction for the two LoDs considered in this paper. To compare this, we use the TUD-campus case, in which the risk map is calculated. In the figures below, the risk map calculated for LoD 1.2 is compared against the one calculated for LoD 2.2 with increasing values of α and β. For increasing values of α the region predicted to be above the 50% mark shrinks, which is not surprising since the area corresponding to a relatively larger non-dimensional velocity shrinks. For the same value of α and increasing values of β, a similar reduction in the risk map is observed since the regions with relatively large non-dimensional velocity and TKE shrink in size. Figs. A.13–A.14 exhibit a constant under-prediction by LoD 1.2 in the risk region when compared to LoD 2.2, further supporting the utility of the joint probability distribution as a useful metric to quantify the similarities and differences observed for this case.

For small values of $\beta < 0.04$, the risk map classifies most of the area as high-risk, mainly because of the smallness of the parameter, such that all grid points return a positive value. This is especially true for $\alpha < 0.4$, where most, if not all, of the area presented in the figures below is classified as high-risk. Since small values of β introduce this consistent bias, the choice for $\alpha = 0.4$ and $\beta = 0.08$ was made in this work to quantify the differences between the two LoDs. It is important to note that this choice must be made with care, is not a generalisation for other urban geometries, and only serves to compare the two different LoDs.

Data availability

Data will be made available on request.

References

Biljecki, F., & Chow, Y. S. (2022). Global building morphology indicators. *Computers, Environment and Urban Systems*, *95*, Article 101809.

Biljecki, F., Ledoux, H., & Stoter, J. (2016). An improved lod specification for 3d building models. *Computers, Environment and Urban Systems*, *59*, 25–37.

Blocken, B. (2015). Computational fluid dynamics for urban physics: Importance, scales, possibilities, limitations and ten tips and tricks towards accurate and reliable simulations. *Building and Environment*, *91*, 219–245.

Boeing, G. (2018). Measuring the complexity of urban form and design. *URBAN DESIGN International*, *23*, 281–292.

Bou-Zeid, E., Overney, J., Rogers, B., & Parlange, M. (2009). The effects of building representation and clustering in large-eddy simulations of flows in urban canopies. *Boundary-Layer Meteorol*, *132*.

C. of the European Union (2023). Fit for 55: Council adopts regulation on CO2 emissions for new cars and vans. https://www.consilium.europa.eu/en/press/press-releases/2023/03/28/fit-for-55-council-adopts-regulation-on-co2-emissions-for-new-cars-and-vans/pdf/, OJ L 200 10.8.2023.

Carpentieri, M., & Robins, A. G. (2015). Influence of urban morphology on air flow over building arrays. *Journal of Wind Engineering and Industrial Aerodynamics*, *145*, 61–74.

Celik, I. B., Ghia, U., Roache, P. J., & Freitas, C. J. (2008). Procedure for estimation and reporting of uncertainty due to discretization in cfd applications. *Journal of Fluids Engineering-Transactions of the ASME*, *130*.

Cho, N., Lee, S., Kim, J., Kim, Y., Park, S., & Song, C. (2019). Wind compensation framework for unpowered aircraft using online waypoint correction. *IEEE Transactions on Aerospace and Electronic Systems*, *56*, 698–710.

Ciarlatani, M. F., Huang, Z., Philips, D., & Gorlé, C. (2023). Investigation of peak wind loading on a high-rise building in the atmospheric boundary layer using large-eddy simulations. *Journal of Wind Engineering and Industrial Aerodynamics*, *236*, Article 105408.

Collett, R. S., & Oduyemi, K. (1997). Air quality modelling: a technical review of mathematical approaches. *Meteorological Applications*, *4*, 235–246.

Cui, S., Yang, Y., Gao, K., Cui, H., & Najafi, A. (2024). Integration of uavs with public transit for delivery: Quantifying system benefits and policy implications. *Transportation Research Part A: Policy and Practice*, *183*, Article 104048.

Davenport, A. G. (1960). Rationale for determining design wind velocities. *Journal of the Structural Division*, *86*, 39–68.

Delft High Performance Computing Centre (DHPC) (2024). Delft blue supercomputer (phase 2).

DJI FlyCart 30 combo. (2025). https://store.dji.bg/en/dji-flycart-30-combo.html (Accessed 02 July 2025).

Elsayed, M., & Mohamed, M. (2020). The impact of airspace regulations on unmanned aerial vehicles in last-mile operation. *Transportation Research Part D: Transport and Environment*, *87*, Article 102480.

Federal Aviation Administration (2024). *Engineering brief no. 105a: vertiport design, supplemental guidance to advisory circular 150/5390-2d, heliport design*. U.S. Department of Transportation, https://www.faa.gov/airports/engineering/engineering_briefs/eb_105a_vertiports.

Fleischmann, M., Romice, O., & Porta, S. (2021). Measuring urban form: Overcoming terminological inconsistencies for a quantitative and comprehensive morphologic analysis of cities. *EPB: Urban Analytics and City Science*, *48*, 2133–2150.

Fowler, D., Brimblecombe, P., Burrows, J., Heal, M. R., Grennfelt, P., Stevenson, D. S., et al. (2020). A chronology of global air quality: The development of global air pollution. *Philosophical Transactions of the Royal Society A: Mathematical, Physical and Engineering Sciences*, *378*.

Franke, J., Hellsten, A., Schlunzen, K. H., & Carissimo, B. (2011). The cost 732 best practice guideline for cfd simulation of flows in the urban environment: a summary. *International Journal of Environment and Pollution*, *44*, 419–427.

Fu, R., Pađen, I., & García-Sánchez, C. (2024). Should we care about the level of detail in trees when running urban microscale simulations? *Sustainable Cities and Society*, *101*, Article 105143.

Galkin, B., Kibilda, J., & DaSilva, L. A. (2019). Uavs as mobile infrastructure: Addressing battery lifetime. *IEEE Communications Magazine*, *57*, 132–137.

Gao, M., Hugenholtz, C. H., Fox, T. A., Kucharczyk, M., Barchyn, T. E., & Nesbit, P. R. (2021). Weather constraints on global drone flyability. *Scientific Reports*, *11*, 12092. http://dx.doi.org/10.1038/s41598-021-91325-w.

García-Sánchez, C., van Beeck, J., & Gorlé, C. (2018). Predictive large eddy simulations for urban flows: Challenges and opportunities. *Building and Environment*, *139*, 146–156.

García-Sánchez, C., Philips, D., & Gorlé, C. (2014). Quantifying inflow uncertainties for cfd simulations of the flow in downtown oklahoma city. *Building and Environment.-Oxford*, *78*, 118–129.

Georegister, D. N. (2025). Platform for high-quality geodata. https://www.pdok.nl/ (Accessed 12 July 2025).

Güneralp, B., Reba, M., Hales, B. U., Wentz, E. A., & Seto, K. C. (2020). Trends in urban land expansion, density, and land transitions from 1970 to 2010: a global synthesis. *Environmental Research Letters*, *15*, Article 044015.

Hagbo, T. O., & Giljarhus, K. E. T. (2022). Pedestrian wind comfort assessment using computational fluid dynamics simulations with varying number of wind directions. *Frontiers in Built Environment*, *8*, Article 858067.

Hang, J., Sandberg, M., & Li, Y. (2009). Effect of urban morphology on wind condition in idealized city models. *Atmospheric Environment*, *43*, 869–878.

Hertwig, D., Efthimiou, G. C., Bartzis, J. G., & Leitl, B. (2012). Cfd-rans model validation of turbulent flow in a semi-idealized urban canopy. *Journal of Wind Engineering and Industrial Aerodynamics*, *111*, 61–72.

Hochschild, J., & Gorlé, C. (2024a). Comparison of measured and les-predicted wind pressures on the space needle. *Journal of Wind Engineering and Industrial Aerodynamics*, *249*, Article 105749.

Hochschild, J., & Gorlé, C. (2024b). Design and demonstration of a sensing network for full-scale wind pressure measurements on buildings. *Journal of Wind Engineering and Industrial Aerodynamics*, *250*, Article 105760.

Hågbo, T.-O., & Giljarhus, K. E. T. (2024). Sensitivity of urban morphology and the number of cfd simulated wind directions on pedestrian wind comfort and safety assessments. *Building and Environment*, *253*, Article 111310.

Hui, Y., Tang, Y., Yang, Q., & Mochida, A. (2024). Numerical study on influence of surface vegetation on aerodynamics of high-rise buildings. *Sustainable Cities and Society*, *107*, Article 105407.

Karimimoshaver, M., Khalvandi, R., & Khalvandi, M. (2021). The effect of urban morphology on heat accumulation in urban street canyons and mitigation approach. *Sustainable Cities and Society*, *73*, Article 103127.

Labetski, A., Vitalis, S., Biljecki, F., Ohori, K. A., & Stoter, J. (2023). 3D building metrics for urban morphology. *International Journal of Geographical Information Science*, *37*, 36–67.

Launder, B., & Spalding, D. (1974). The numerical computation of turbulent flows. *Computer Methods in Applied Mechanics and Engineering*, *3*, 269–289.

Lawson, T. (1978). The wind content of the built environment. *Journal of Wind Engineering and Industrial Aerodynamics*, *3*, 93–105.

Lemardelé, C., Estrada, M., Pagès, L., & Bachofner, M. (2021). Potentialities of drones and ground autonomous delivery devices for last-mile logistics. *Transportation Research Part E*, *149*, 1366–5545.

McDonald, R. I., Mansur, A. V., Ascensão, F., Colbert, M., Crossman, K., Elmqvist, T., et al. (2020). Research gaps in knowledge of the impact of urban growth on biodiversity. *Nature Sustainability*, *3*, 16–24.

Mirzaei, P. A. (2021). Cfd modeling of micro and urban climates: Problems to be solved in the new decade. *Sustainable Cities and Society*, *69*, Article 102839.

Moonen, P., Dorer, V., & Carmeliet, J. (2011). Evaluation of the ventilation potential of courtyards and urban street canyons using rans and les. *Journal of Wind Engineering and Industrial Aerodynamics*, *99*, 414–423.

Muia, M. J., Stanley, J., Anderson, T., Hall, D., Shuman, Z., Goericke, J., et al. (2024). In William J. Hughes (Ed.), *Electric vertical takeoff and landing (EVTOL) downwash and outwash surveys*: *Technical Report DOT/FAA/TC-24/42*, Technical Center, Washington, DC: Federal Aviation Administration, http://dx.doi.org/10.21949/5hy5-z760, URL: https://vast.aero/wp-content/uploads/2025/01/eVTOL-Downwash-and-Outwash-Surveys.pdf.

Nagl, C., Buxbaum, I., Bohmer, S., Ibesich, N., & Mendoza, H. R. (2018). *Air quality and urban traffic in the EU: best practices and possible solutions*: *Technical Report*, Umweltbundesamt (Austria: (Accessed 16 2024).

Nazarian, N., Krayenhoff, E. S., & Martilli, A. (2020). A one-dimensional model of turbulent flow through urban canopies (MLUCM v2.0): updates based on large-eddy simulation. *Geoscientific Model Development*, *13*, 937–953. http://dx.doi.org/10.5194/gmd-13-937-2020, URL: https://gmd.copernicus.org/articles/13/937/2020/.

NEN, W. C. (2006). *Wind danger in the built environment*. Delft, The Netherlands: Netherland's Standardization Institute.

OpenStreetMap contributors (2017). OpenStreetMap contributors planet dump. retrieved from https://planet.osm.org (Accessed 19 2024).

Pađen, I., García-Sánchez, C., & Ledoux, H. (2022). Towards automatic reconstruction of 3d city models tailored for urban flow simulations. *Frontiers in Built Environment*, *8*, Article 899332.

Pađen, I., Peters, R., García-Sánchez, C., & Ledoux, H. (2024). Automatic high-detailed building reconstruction workflow for urban microscale simulations. *Building and Environment*, *265*, Article 111978.

Palusci, O., Monti, P., Cecere, C., Montazeri, H., & Blocken, B. (2021). Impact of morphological parameters on urban ventilation in compact cities: The case of the tuscolano-don bosco district in rome. *Science of the Total Environment*.

Parente, A., Gorlé, C., van Beeck, J., & Benocci, C. (2011). Improved $k-\epsilon$ model and wall function formulation for the rans simulation of abl flows. *Journal of Wind Engineering and Industrial Aerodynamics*, *99*, 267–278, The Fifth International Symposium on Computational Wind Engineering..

Patankar, S. (1980). *Numerical heat transfer and fluid flow* (1st ed.). Boca Raton, Florida: CRC Press.

Peskin, C. S. (2002). The immersed boundary method. *Acta Numerica*, *11*, 479–517.

Peters, R., Dukai, B., Vitalis, S., van Liempt, J., & Stoter, J. (2022). Automated 3d reconstruction of lod2 and lod1 models for all 10 million buildings of the netherlands. *Photogrammetric Engineering and Remote Sensing*, *88*, 165–170.

Pomaranzi, G., Amerio, L., Schito, P., Lamberti, G., Gorlé, C., & Zasso, A. (2022). Wind tunnel pressure data analysis for peak cladding load estimation on a high-rise building. *Journal of Wind Engineering and Industrial Aerodynamics*, *220*, Article 104855.

Salim, S. M., Buccolieri, R., Chan, A., & Di Sabatino, S. (2011). Numerical simulation of atmospheric pollutant dispersion in an urban street canyon: Comparison between rans and les. *Journal of Wind Engineering and Industrial Aerodynamics*, *99*, 103–113.

Sanz-Andres, A., & Cuerva, A. (2006). Pedestrian wind comfort: Feasibility study of criteria homogenisation. *Journal of Wind Engineering and Industrial Aerodynamics*, *94*, 799–813.

Shirzadi, M., Tominaga, Y., & Mirzaei, P. A. (2020). Experimental and steady-rans cfd modelling of cross-ventilation in moderately-dense urban areas. *Sustainable Cities and Society*, *52*, Article 101849.

Tran, V. P., Santoso, F., & Garratt, M. A. (2021). Adaptive trajectory tracking for quadrotor systems in unknown wind environments using particle swarm optimization-based strictly negative imaginary controllers. *IEEE Transactions on Aerospace and Electronic Systems*, *57*, 1742–1752.

van der Vaart, J., Stoter, J., Diakité, A., Biljecki, F., Ohori, K. A., & Hakim, A. (2024). Assessment of the lod specification for the integration of bim-derived building models in 3d city models. *Lecture Notes in Geoinformation and Cartography*, 171–191.

Weller, H. G., Tabor, G., Jasak, H., & Fureby, C. (1998). A tensorial approach to computational continuum mechanics using object-oriented techniques. *Computer in Physics*, *12*, 620–631.

Wieringa, J. (1992). Updating the davenport roughness classification. *Journal of Wind Engineering and Industrial Aerodynamics*, *41*, 357–368.

Wolf, T., Pettersson, L. H., & Esau, I. (2020). A very high-resolution assessment and modelling of urban air quality. *Atmospheric Chemistry and Physics*, *20*, 625–647.

Xing, Z., Zhang, Y., & Su, C.-Y. (2023). Active wind rejection control for a quadrotor uav against unknown winds. *IEEE Transactions on Aerospace and Electronic Systems*, *59*, 8956–8968.

YouTube (2023). YouTube trotseer wind bij faculteit EWI at TU delft. YouTube URL: https://youtu.be/U6QtxJNhiog Video.

Zhang, W., Zhu, X., Yang, X. I. A., & Wan, M. (2022). Evidence for raupach, others, 's mixing-layer analogy in deep homogeneous urban-canopy flows. *Journal of Fluid Mechanics*, *944*, A46. http://dx.doi.org/10.1017/jfm.2022.507.